Near-Field Thermal Radiation between Nanostructures of Natural Anisotropic Material

Jiadong Shen,[1] Xianglei Liu,[1,2,*] and Yimin Xuan[1,2]

[1]*School of Energy and Power Engineering, Nanjing University of Aeronautics and Astronautics, Nanjing 210016, China*

[2]*Aero-engine Thermal Environment and Structure Key Laboratory of Ministry of Industry and Information Technology, Nanjing 210016, China*

(Received 11 April 2018; revised manuscript received 25 May 2018; published 17 September 2018)

Nanostructures have exhibited unprecedented optical and thermal properties including super-Planckian thermal radiation. Nevertheless, nanostructures are usually made of isotropic materials while anisotropic counterparts are rarely considered despite their wide applications. This paper investigates near-field thermal radiation between gratings consisting of natural anisotropic graphite. Graphite gratings with optical axes lying out of plane are found to possess sevenfold larger radiative heat flux than counterpart plane plates at nanoscale gap distances, outperforming blackbodies by over four orders of magnitude. The dominant radiative heat transfer channel changes from nonresonant hyperbolic modes to anisotropic surface resonant modes after patterning. The strong coupling of anisotropic surface modes with high k waves in a broad frequency range results in the extremely efficient radiative heat transfer of graphite gratings. This work helps deepen the understanding of thermal radiation of anisotropic nanostructures and opens routes for more efficient thermal radiative transport.

DOI: 10.1103/PhysRevApplied.10.034029

I. INTRODUCTION

Patterning materials into nanostructures, e.g., nanowires, nanotubes, multilayers, and gratings, has opened ways to realize unprecedented electrical, optical, and thermal properties. These extraordinary characteristics enable a plethora of exciting applications, such as optical cloaking [1], negative refraction [2], and extremely high thermal conductivity [3], to name a few. In particular, thermal radiation, as one of the most universal phenomena in the world, can be dramatically tuned via nanopatterning. By employing nanostructures, exotic radiative properties such as perfect omnidirectional absorption [4,5], coherent emission [6], and daytime radiative cooling [7] have been demonstrated, which are hardly possible for bulk counterparts. In addition to the promising far-field radiative properties mentioned above, similar phenomena may apply to the near-field thermal radiation (NFTR) as well due to the exotic interaction of light with nanostructures.

As has been theoretically and experimentally investigated, when two objects of different temperatures are separated by a submicrometer gap distance, the otherwise trivial tunneling of evanescent electromagnetic waves can render radiative heat exchange to surpass the blackbody limit [8–20]. Due to this efficient energy transfer, NFTR has received much attention in wide applications, such as noncontact thermal management, heat-to-electricity conversion, thermal modulation, subwavelength thermal imaging, etc. [21–34]. In particular, nanostructures have recently been demonstrated to be able to further enhance the near-field radiative heat exchange, improve the energy conversion efficiency, and increase the modulation contrast [35–45]. For example, Guérout *et al*. [35] explored the NFTR between one-dimensional gold gratings, and achieved an enhanced radiative heat transfer over counterpart plates, which is ascribed to the presence of additional guide modes in the thermal frequency window. Watjen *et al*. [46] corrugated a tungsten emitter into gratings and paired it with an $In_{0.82}Ga_{0.18}Sb$ thermophotovoltaic cell. They observed that the energy transmission coefficient can be enhanced, especially near the bandgap, so that the power output and energy conversion efficiency could be improved over the counterpart planar scheme by 40% and 2.1%, respectively. By employing the mechanical rotation between two misaligned gratings in close proximity, Biehs *et al*. [47] and Liu *et al*. [27] designed noncontact thermal modulators with modulation contrasts as high as 5. Previous investigations only consider nanostructures made of isotropic materials, while natural anisotropic materials have recently triggered intense attention in the fields of plasmonics, optoelectronics, and thermal management. However, in stark contrast, NFTR between nanostructures consisting of natural anisotropic materials has not been reported. What radiative properties nanostructures

*xliu@nuaa.edu.cn

 © 2018 American Physical Society

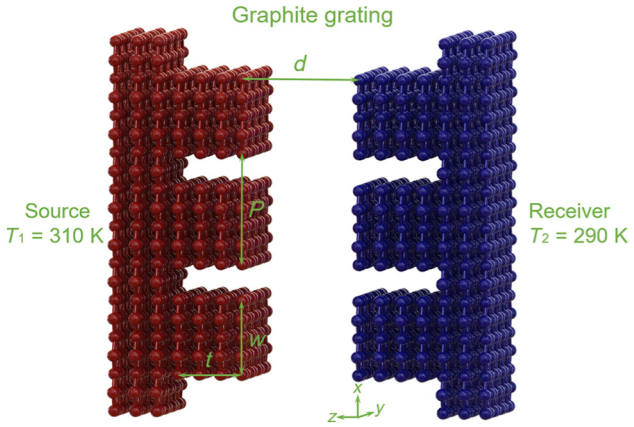

FIG. 1. Schematic of near-field thermal radiation between aligned gratings of graphite with optical axis out of plane (z coordinate), separated by a vacuum gap d. Grating filling factor f is defined as the ratio of width W to the period P. Temperatures $T_1 = 310$ K and $T_2 = 290$ K are set as default.

consisting of natural anisotropic materials will exhibit in the near field is still an open question. In order to fill in the blanks, this paper investigates the NFTR between nanostructures comprised of natural anisotropic materials, i.e., graphite with different orientations of the optical axis. Based on exact scattering theories, graphite gratings are found to support higher radiative heat flux when the optical axis lies out of plane compared with the scenario of being in plane. For the former scheme, with a filling factor of 0.1, the radiative heat exchange between graphite gratings is predicted to be sevenfold higher than that between counterpart plane plates at nanoscale gap distances and periods, outperforming the blackbody limit by more than four orders of magnitude. The underlying physical mechanism will be discussed later.

II. THEORETICAL FORMULATION

Graphite, a natural anisotropic material comprised of layered hexagonal arrays of carbon atoms, is selected for investigation in this paper due to its many applications in thermal management and electronic industries. Other natural anisotropic materials, e.g., hexagonal boron nitride and black phosphorous, can also be explored via this method in the future. Figure 1 depicts the schematic of NFTR between aligned gratings of graphite with the optical axis out of plane (i.e., along the z coordinate, set as default unless otherwise specified), separated by a vacuum gap d. The patterning direction is always along the x axis. The dimension along the y axis is assumed to be infinite, i.e., a one-dimensional (1D) grating. The thickness of gratings t is taken to be sufficiently large to simplify analyses unless they are specified. Grating filling factor f is defined as the ratio of grating width W to the period P. The temperatures of gratings are set to be $T_1 = 310$ K and $T_2 = 290$ K as the defaults.

By employing the exact scattering theory based on rigorous coupled-wave analysis (RCWA), near-field radiative heat flux (N-FRHF) between periodic nanostructures can be described as [35]

$$Q = \frac{1}{8\pi^3}\int_0^\infty [\Theta(\omega, T_H) - \Theta(\omega, T_L)]d\omega \int_{-\infty}^{\infty}\int_{-\pi/P}^{\pi/P} \xi(\omega, k_x, k_y)dk_x dk_y \tag{1}$$

where $\Theta(\omega, T) = \hbar\omega/(e^{\hbar\omega/k_B T} - 1)$ represents the mean energy of Plank's oscillator. k_x and k_y denote tangential wavevectors along the x and y axes, respectively. Due to the periodicity in the x direction, k_x is integrated from $-\pi/P$ to π/P. $\xi(\omega, k_x, k_y)$ is the energy transmission coefficient depending on the reflection coefficient matrix of the nanostructures. The derivation of the reflection coefficient matrix for gratings made of anisotropic materials with $\varepsilon = \mathrm{diag}(\varepsilon_x, \varepsilon_y, \varepsilon_z)$ is given briefly as follows. For an incident wave with a wavevector of $k_i^{(p)} = (k_x^{(p)}, k_y, -k_z^{(i,p)})$, the fields in the vacuum can be written as

$$E_y(x,z) = \sum_{n=-\infty}^{n=+\infty} \delta_{np} I_p^{(e)} e^{i(k_x^{(p)}x - k_z^{(i,p)}z)} + R_{np}^{(e)} e^{i(k_x^{(n)}x + k_z^{(i,n)}z)} \tag{2a}$$

$$H_y(x,z) = \sum_{n=-\infty}^{n=+\infty} \delta_{np} I_p^{(h)} e^{i(k_x^{(p)}x - k_z^{(i,p)}z)} + R_{np}^{(h)} e^{i(k_x^{(n)}x + k_z^{(i,n)}z)} \tag{2b}$$

The x components of the fields can be derived from their y components by employment of the Maxwell's curl equations. The fields inside gratings can also be described as Rayleigh expansions, and then the Fourier components of the fields $\mathbf{F} = (\mathrm{e_x}, \mathrm{e_y}, \mathrm{h_x}, \mathrm{h_y})^T$ can be written as

$$\partial_z \mathbf{F} = \mathbf{M}\mathbf{F}$$

$$\mathbf{M} = \begin{pmatrix} \mathbf{0} & \mathbf{0} & -\frac{ik_y}{\omega}\mathbf{k_x}\epsilon_\mathbf{z}^{-1} & -i\omega\mathbf{1} + \frac{i}{\omega}\mathbf{k_x}\epsilon_\mathbf{z}^{-1}\mathbf{k_x} \\ \mathbf{0} & \mathbf{0} & i\omega\mathbf{1} - \frac{ik_y^2}{\omega}\epsilon_\mathbf{z}^{-1} & \frac{ik_y}{\omega}\epsilon_\mathbf{z}^{-1}\mathbf{k_x} \\ \frac{ik_y}{\omega}\mathbf{k_x} & i\omega\epsilon_\mathbf{y} - \frac{i}{\omega}\mathbf{k_x}\mathbf{k_x} & \mathbf{0} & \mathbf{0} \\ -i\omega\epsilon_\mathbf{x} + \frac{ik_y^2}{\omega}\mathbf{1} & -\frac{ik_y}{\omega}\mathbf{k_x} & \mathbf{0} & \mathbf{0} \end{pmatrix} = \begin{pmatrix} \mathbf{0} & \mathbf{M}_1 \\ \mathbf{M}_2 & \mathbf{0} \end{pmatrix} \tag{3}$$

where $\mathbf{k_x} = \mathrm{diag}(k_x^n)$ and 1 is the identity matrix. $\mathbf{K_x}$ collects diffracted wavevectors $k_x^n = k_x^p + n(2\pi/P)$, where n runs from $-N$ to N (the highest diffraction order). $\epsilon_\mathbf{i}$ and $\epsilon_\mathbf{i}^{-1}$ are dielectric function tensors and their reciprocals expanded in Fourier series, respectively. The bold quantities in the above larger matrix have dimensions of $2N+1$. Combining the above equations with the boundary condition that the tangential fields across the interface should be conserved, the reflection coefficient matrices $\mathbf{R}^\mathrm{e}$ and $\mathbf{R}^\mathrm{h}$ can be obtained [48].

In addition to exact scattering theory, effective medium theory (EMT), which treats nanostructures of anisotropic materials as equivalent homogenous biaxial plates, is employed to assist the analysis due to its simplicity and rapid calculation speed. The effective dielectric function of nanostructures can be written as $\varepsilon_\mathrm{eff} = \mathrm{diag}(\varepsilon_{\mathrm{eff},x}, \varepsilon_{\mathrm{eff},y}, \varepsilon_{\mathrm{eff},z})$, where $\varepsilon_{\mathrm{eff},x} = \varepsilon_o/[f + (1-f)\varepsilon_o]$, $\varepsilon_{\mathrm{eff},y} = f\,\varepsilon_o + 1 - f$, and $\varepsilon_{\mathrm{eff},z} = f\,\varepsilon_e + 1 - f$. Parameters ε_o and ε_e represent the dielectric functions for ordinary and extraordinary waves, respectively. The dielectric function of graphite is obtained from Refs. [49] and [50]. Elaborate derivations of reflection coefficients of biaxial media can be found in Ref. [51]. Here, we give the longitudinal wavevector in biaxial media as [51]

$$k_z^{(m)} = \frac{\omega}{\sqrt{2}}\sqrt{A + B \pm \sqrt{(A-B)^2 + 4C}} \tag{4}$$

where $A = L_{14}L_{41}$, $B = L_{23}L_{32}$, and $C = C_1C_2 = L_{14}L_{42} \times L_{23}L_{31}$. $m = 1$ or 2, meaning birefraction. L_{ij} is an element of the matrix $\mathbf{L}$ expressed as

$$\mathbf{L} = \begin{pmatrix} 0 & 0 & 0 & \dfrac{\beta^2}{\omega^2\varepsilon_0\varepsilon_{\mathrm{eff},z}} - \mu_0 \\ 0 & 0 & \mu_0 & 0 \\ \varepsilon_0(\varepsilon_{\mathrm{eff},x} - \varepsilon_{\mathrm{eff},y})\sin\varphi\cos\varphi & \varepsilon_0(\varepsilon_{\mathrm{eff},x}\sin^2\varphi + \varepsilon_{\mathrm{eff},y}\cos^2\varphi) - \dfrac{\beta^2}{\omega^2\mu_0} & 0 & 0 \\ -\varepsilon_0(\varepsilon_{\mathrm{eff},x}\cos^2\varphi + \varepsilon_{\mathrm{eff},y}\sin^2\varphi) & -\varepsilon_0(\varepsilon_{\mathrm{eff},x} - \varepsilon_{\mathrm{eff},y})\sin\varphi\cos\varphi & 0 & 0 \end{pmatrix} \tag{5}$$

where $\beta = \sqrt{k_x^2 + k_y^2}$ is the tangential wavevector along the x-y plane. ε_0 and μ_0 are the permittivity and permeability in the vacuum, respectively. $\varphi = \arccos(k_x/\beta)$ represents the circumferential angle. The reflection coefficients for biaxial media are computed as

$$r_s^s = \frac{\frac{k_{0z}}{\omega\varepsilon_0}(\beta^{(1)}\gamma^{(2)} - \beta^{(2)}\gamma^{(1)}) + (\beta^{(1)} - \beta^{(2)}) + \frac{k_{0z}^2}{\omega^2\varepsilon_0\mu_0}(\alpha^{(1)}\gamma^{(2)} - \alpha^{(2)}\gamma^{(1)}) + \frac{k_{0z}}{\omega\mu_0}(\alpha^{(1)} - \alpha^{(2)})}{\frac{k_{0z}}{\omega\varepsilon_0}(\beta^{(2)}\gamma^{(1)} - \beta^{(1)}\gamma^{(2)}) + (\beta^{(2)} - \beta^{(1)}) + \frac{k_{0z}^2}{\omega^2\varepsilon_0\mu_0}(\alpha^{(1)}\gamma^{(2)} - \alpha^{(2)}\gamma^{(1)}) + \frac{k_{0z}}{\omega\mu_0}(\alpha^{(1)} - \alpha^{(2)})}, \tag{6a}$$

$$r_s^p = \frac{\frac{2k_{0z}}{\omega\mu_0}(\gamma^{(1)} - \gamma^{(2)})}{\frac{k_{0z}}{\omega\varepsilon_0}(\beta^{(2)}\gamma^{(1)} - \beta^{(1)}\gamma^{(2)}) + (\beta^{(2)} - \beta^{(1)}) + \frac{k_{0z}^2}{\omega^2\varepsilon_0\mu_0}(\alpha^{(1)}\gamma^{(2)} - \alpha^{(2)}\gamma^{(1)}) + \frac{k_{0z}}{\omega\mu_0}(\alpha^{(1)} - \alpha^{(2)})}, \tag{6b}$$

$$r_p^s = \frac{\frac{2k_{0z}}{\omega\varepsilon_0}(\alpha^{(1)}\beta^{(2)} - \alpha^{(2)}\beta^{(1)})}{\frac{k_{0z}}{\omega\varepsilon_0}(\beta^{(2)}\gamma^{(1)} - \beta^{(1)}\gamma^{(2)}) + (\beta^{(2)} - \beta^{(1)}) + \frac{k_{0z}^2}{\omega^2\varepsilon_0\mu_0}(\alpha^{(1)}\gamma^{(2)} - \alpha^{(2)}\gamma^{(1)}) + \frac{k_{0z}}{\omega\mu_0}(\alpha^{(1)} - \alpha^{(2)})}, \tag{6c}$$

$$r_p^p = \frac{\frac{k_{0z}}{\omega\varepsilon_0}(\beta^{(2)}\gamma^{(1)} - \beta^{(1)}\gamma^{(2)}) + (\beta^{(1)} - \beta^{(2)}) + \frac{k_{0z}^2}{\omega^2\varepsilon_0\mu_0}(\alpha^{(1)}\gamma^{(2)} - \alpha^{(2)}\gamma^{(1)}) + \frac{k_{0z}}{\omega\mu_0}(\alpha^{(2)} - \alpha^{(1)})}{\frac{k_{0z}}{\omega\varepsilon_0}(\beta^{(2)}\gamma^{(1)} - \beta^{(1)}\gamma^{(2)}) + (\beta^{(2)} - \beta^{(1)}) + \frac{k_{0z}^2}{\omega^2\varepsilon_0\mu_0}(\alpha^{(1)}\gamma^{(2)} - \alpha^{(2)}\gamma^{(1)}) + \frac{k_{0z}}{\omega\mu_0}(\alpha^{(1)} - \alpha^{(2)})}, \tag{6d}$$

where $\alpha^{(m)} = [((k_z^{(m)})^2 - \omega^2 A)/\omega^2 C_1]$, $\beta^{(m)} = -(k_z^{(m)}\alpha^{(m)}/\omega\mu_0)$, and $\gamma^{(m)} = -(k_z^{(m)}/\omega L_{14})$. $k_{0z} = \sqrt{k_0^2 - \beta^2}$ is the longitudinal wavevector in the vacuum.

Zeroing the denominator of reflection coefficients, the dispersion relation of anisotropic surface resonant modes can be obtained as

$$(\beta^2 - \varepsilon_{\mathrm{eff},z}k_0^2)[(k_z^{(1)})^2 + k_z^{(1)}k_z^{(2)} + (k_z^{(2)})^2] + (\beta^2 k_{0z} - \varepsilon_{\mathrm{eff},z}k_0^2 k_{0z} - \varepsilon_{\mathrm{eff},z}k_{0z}k_z^{(1)}k_z^{(2)}) \times [k_z^{(1)} + k_z^{(2)}] - (\omega^2 A\beta^2 - \omega^2 A\varepsilon_{\mathrm{eff},z}k_0^2 + \omega^2 A\varepsilon_{\mathrm{eff},z}k_{0z}^2 + \varepsilon_{\mathrm{eff},z}k_{0z}^2 k_z^{(1)}k_z^{(2)}) = 0. \quad (7)$$

When $\beta \gg k_0$, $k_{0z} \approx i\beta$. $A \times B$ and C in Eq. (4) are proportional to β to the fourth and second powers, respectively. Thus, C can be ignored, $k_z^{(1)} \approx \omega\sqrt{A}$, and $k_z^{(2)} \approx \omega\sqrt{B}$. Subsequently, Eq. (7) can be simplified as

$$\beta^2 - \omega^2\varepsilon_{\mathrm{eff},z}\sqrt{AB} - i\omega\beta(\varepsilon_{\mathrm{eff},z}\sqrt{A} + \sqrt{B}) = 0 \quad (8)$$

Note that there exist four combination modes of $\sqrt{A}$ and $\sqrt{B}$. Only when $\sqrt{A} \approx -i(\beta/\omega\sqrt{\varepsilon_{\mathrm{eff},z}})\sqrt{\varepsilon_{\mathrm{eff},x}\cos^2\varphi + \varepsilon_{\mathrm{eff},y}\sin^2\varphi}$ and $\sqrt{B} = i(\beta/\omega)$, can we achieve meaningful solutions. In consequence, for high-β waves, the asymptote of the dispersion relation of anisotropic surface resonant modes is approximately

$$k_y = \pm k_x\sqrt{\frac{1 - \varepsilon_{\mathrm{eff},x}\varepsilon_{\mathrm{eff},z}}{\varepsilon_{\mathrm{eff},y}\varepsilon_{\mathrm{eff},z} - 1}} \quad (9)$$

For a uniaxial plate with an optical axis in plane, Eq. (9) will degenerate into $k_y = \pm k_x\sqrt{(1 - \varepsilon_o\varepsilon_e)/(\varepsilon_o^2 - 1)}$, which coincides with Eq. (9) in Ref. [52] (the constant $\pm k_0\sqrt{\varepsilon_o^2\varepsilon_e/(\varepsilon_o\varepsilon_e - 1)}$ is negligible compared with k_x for high-β waves). This further verifies Eq. (9) and demonstrates its general applicability.

III. RESULTS AND DISCUSSION

A. Efficient near-field thermal radiation between graphite gratings

Figure 2(a) plots the NFRHF of graphite gratings as a function of filling factors with $P = 10$ nm at $d = 50$ nm. The radiative heat flux is normalized to that of a blackbody ($Q_{\mathrm{BB}} = 123$ W/m^2). As can be clearly seen, patterning graphite plates into 1D gratings enables an augment of thermal radiation for all practical filling factors ($f > 0.005$). Then, the NFRHF decreases monotonically as filling factors increase. This can be interpreted in terms of imaginary parts of the dielectric functions. Approximating graphite gratings as effective homogenous biaxial plates, then $\mathrm{Im}(\varepsilon_{\mathrm{eff},x}) = f\,\mathrm{Im}(\varepsilon_o)/([f + (1-f)\mathrm{Re}(\varepsilon_o)]^2 + (1-f)^2\mathrm{Im}^2(\varepsilon_o))$, $\mathrm{Im}(\varepsilon_{\mathrm{eff},y}) = f\,\mathrm{Im}(\varepsilon_o)$, and $\mathrm{Im}(\varepsilon_{\mathrm{eff},z}) = f\,\mathrm{Im}(\varepsilon_e)$, where $\mathrm{Re}(\varepsilon_o)$ and $\mathrm{Im}(\varepsilon_o)$ are extremely large. From the above equations, we can conclude that decreasing filling factors will lead to a reduction of these imaginary parts. Moderately reducing the imaginary parts of dielectric functions helps to increase the local density of states for both surface modes and nonresonant hyperbolic modes (essentially the frustrated total internal reflection of hyperbolic materials, no resonances are excited), which is beneficial to NFTR [53]. Thus, a smaller filling factor corresponds to a larger NFRHF for graphite gratings. Nevertheless, when f is too small, e.g., below 0.03, the fluctuation current becomes very small according to the fluctuation-dissipation theorem, causing NFTR between graphite gratings to deteriorate dramatically. When f further decreases to zero, i.e., only vacuum exists, the heat transfer will vanish, as shown in the figure. The optimal NFRHF supported by graphite gratings at $f = 0.03$ is about 7.14 times as high as that for counterpart plates, and outperforms the blackbody limit by 276-fold. Without loss of generalities, $f = 0.1$, where

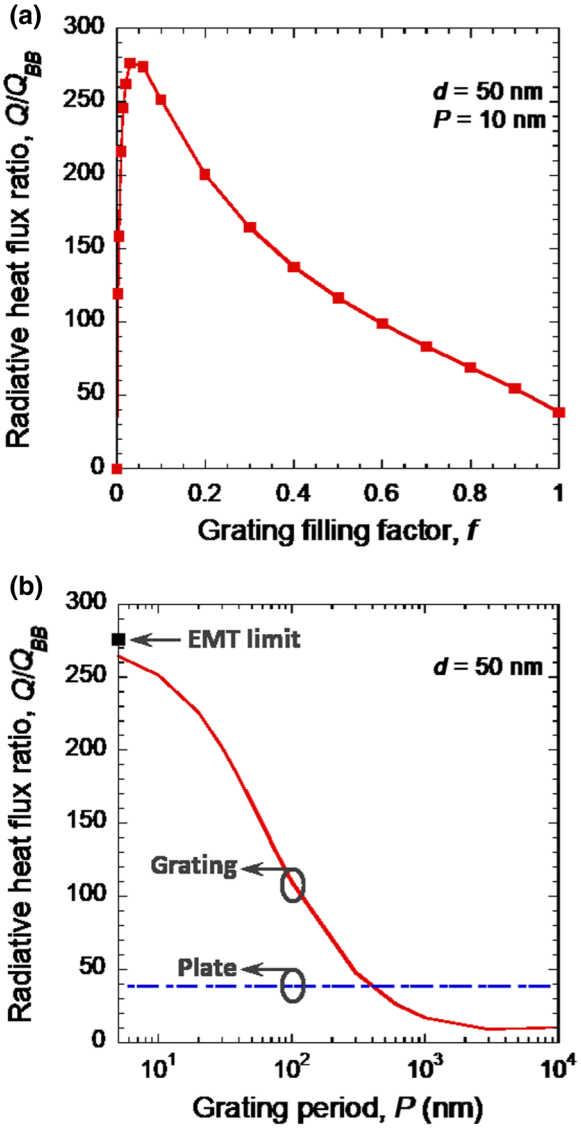

FIG. 2. Radiative heat flux ratio of graphite gratings as a function of (a) filling factors with $P = 10$ nm at $d = 50$ nm; (b) periods with $f = 0.1$ at $d = 50$ nm. The radiative heat flux ratio is normalized to the blackbody limit $Q_{\mathrm{BB}} = 123$ W/m^2.

NFRHF drops slightly from the peak, is selected in further analyses.

The effect of periods on the NFRHF of graphite gratings is illustrated in Fig. 2(b) at the same gap distance as in Fig. 2(a). As denoted by the red solid line, the NFRHF of graphite gratings increases continuously and approaches the value predicted by EMT (delineated by the black square) with decreasing periods. The radiative heat exchange of 32.4 kW/m^2 at $P = 5$ nm is lower than the EMT limit of 33.8 kW/m^2 by 4.1%. The discrepancy will further decrease and even vanish at smaller periods. It is reasonable that electromagnetic waves cannot identify the fine structural details of gratings at extremely small periods, so that those nanostructures can be homogenized as homogeneous plates. As expected, along with the rise in the periods, the NFRHF of graphite gratings will eventually approach the value calculated by proximity approximation (PA) due to the gradually diminishing influence of interactions between nearby unit cells. The upper and lower critical values are governed by the EMT and PA limit [54]. Graphite gratings do not always possess superiorities as compared to counterpart plates represented by the blue dash-dotted line in terms of the NFRHF. They perform better only when the period is below around 400 nm, as shown in the figure. To further demonstrate the performance of graphite gratings without losing generalities, the filling factor of 0.1 and period of 10 nm are chosen as default in the remainder of this paper.

Figure 3(a) depicts the normalized NFRHF of graphite gratings, plane plates, and the ratio between them with varying gap distances while keeping the other parameters fixed at the default values. As represented by the red solid and blue dash-dotted lines, both graphite gratings and plates present a monotonous augment of NFRHF with decreasing gap distances as expected due to the increasing local density of the states. In the deep near field, where the gap distance is smaller than tens of nanometers, the NFRHF of graphite plates follows the power law of d^{-2} due to the dominant contributions of nonresonant hyperbolic modes [55,56] while that of graphite gratings changes more slowly than d^{-2}. As a result, the ratio between the NFRHFs of gratings and plates drops in the deep near field, as shown by the black dot line. When the gap distance approaches around 10 μm, neither the interference of propagating waves nor the tunneling of evanescent waves becomes nontrivial, and the NFRHFs of both graphite gratings and plates saturates there and converges to the far-field values. In terms of the radiative heat transfer enhancement, graphite gratings outperform counterpart plates at any practical gap distances ranging from deep submicron to far field. At $d = 25$ nm, the NFRHF of graphite gratings can be 7.87 times as large as that of counterpart plates. Furthermore, at smaller gap distances, e.g., $d = 5$ nm, the heat exchange between graphite gratings can be higher than the blackbody limit by more than four orders of magnitude, confirming their enormous potential in applications ranging from efficient thermal management to super-Planckian thermophotovoltaic energy conversion.

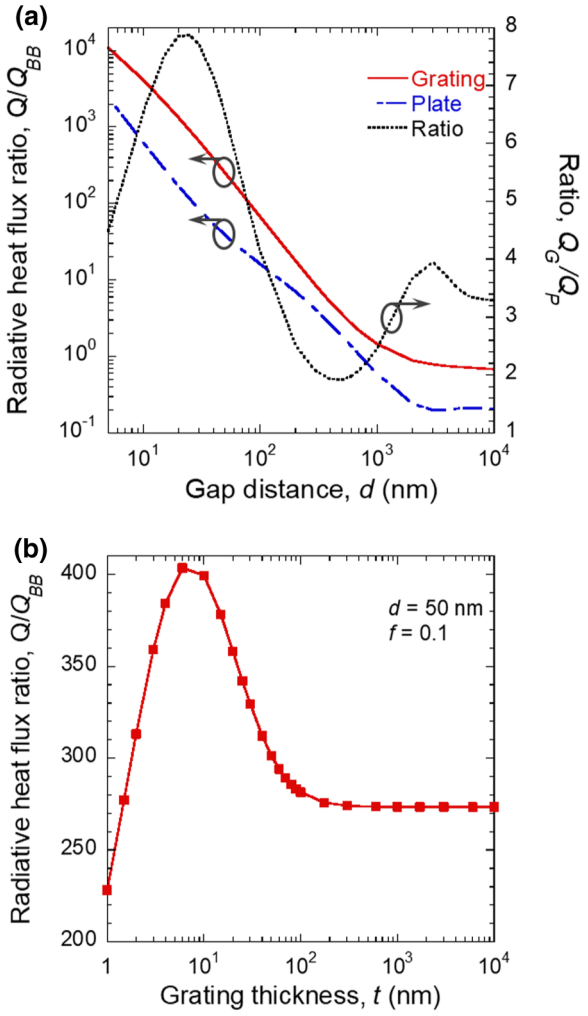

FIG. 3. (a) Effect of gap distances on the near-field thermal radiation of graphite gratings ($f = 0.1$, $P = 10$ nm), plates, and their ratio; (b) Radiative heat flux ratio of graphite gratings with sufficiently small periods varying with grating thicknesses/depths at $f = 0.1$ and $d = 50$ nm.

Figure 3(b) illustrates the effects of grating thicknesses/depths on the NFTR of graphite gratings with $f = 0.1$ at $d = 50$ nm (the backing substrate is the vacuum). To simplify computations, the optimal configuration, i.e., periods are sufficiently small, is chosen, and thus EMT can be employed. As shown in the figure, the NFRHF changes very little and nearly saturates at thicknesses larger than around 100 nm. Thinning gratings (when $t < 100$ nm) can elevate their performance of radiative heat transfer in the near field. The NFRHF of thin graphite gratings peaks at $t = 6$ nm, with a value higher than that of bulk counterparts by 47.7%. Similar phenomena have already been observed for both thin plane plates

and 1D gratings due to the coupling of surface resonances inside the film [9,57]. As thicknesses further decrease, the NFTR between thin graphite gratings deteriorates dramatically. This is reasonable because with grating thicknesses dropping to zero, i.e., only the vacuum exists, the heat exchange would vanish. To simplify the following analyses of heat transfer mechanism, bulk gratings are selected as the default.

B. Underlying mechanism of high near-field thermal radiation between graphite gratings

To facilitate the mechanism analysis, the effective dielectric functions (real parts only) of graphite gratings with $f = 0.1$ are plotted in Fig. 4(a). As demonstrated in previous literature [49,50,58], graphite plates can support broadband Type II hyperbolic dispersion in the infrared region. In addition to uniaxial materials, hyperbolic bands can exist in other types of materials as long as the dispersion curves are hyperbolic [59]. When $k_x, k_y \gg k_0$, one of the longitudinal wavevectors in effective biaxial graphite gratings can be simplified as $k_z^{(1)} \approx \omega\sqrt{A} = -i(\beta/\sqrt{\varepsilon_{\mathrm{eff},z}})\sqrt{\varepsilon_{\mathrm{eff},x}\cos^2\varphi + \varepsilon_{\mathrm{eff},y}\sin^2\varphi}$. Thus, the dispersion relation of biaxial graphite gratings can be written as $\varepsilon_{\mathrm{eff},x}k_x^2 + \varepsilon_{\mathrm{eff},y}k_y^2 + \varepsilon_{\mathrm{eff},z}k_z^2 = 0$. As shown in Fig. 4(a), only $\varepsilon_{\mathrm{eff},y}$ is negative, then the above dispersion curve graphs shape as a hyperboloid. This can be verified by the hyperbolic isofrequency surface at $\omega = 1.3 \times 10^{14}$ rad/s shown in Fig. 4(b). The dispersion relation curve for biaxial hyperbolic materials at the k_x-k_z plane is an ellipse, while for uniaxial hyperbolic materials, it is a circle. This is the main difference of material dispersions between uniaxial and biaxial hyperbolic materials. Although still possessing hyperbolic bands, patterning significantly alters graphite's optical response and renders it to become a Type I hyperbolic metamaterial (only one component of the dielectric tensor is negative). In order to explain the underlying mechanism of the excellent performance of graphite gratings without losing generalities, $d = 50$ nm is selected. Figure 4(c) gives the spectral radiative heat flux (SRHF) of graphite gratings and plates. The default parameters of the grating, i.e., $f = 0.1$ and $P = 10$ nm, are used. As can been seen in the figure, the SRHF of graphite gratings denoted by the red solid line is much higher than that of the counterpart plates represented by the blue dot line within the whole frequency region. This enables graphite gratings to harvest a 5.5-fold larger NFRHF. For graphite gratings, the vast majority of SRHF concentrates on the Type I hyperbolic bands, contributing 83.5% (25.75 kW/m^2/30.82 kW/m^2), as delineated by the light blue shaded regions. Note that corrugating graphite plates not only enhances and redshifts the peak SRHF from 8.1×10^{13} to 5.6×10^{13} rad/s in the high-frequency hyperbolic band, but also gives rise to another peak SRHF at 1.6×10^{13} rad/s in the low-frequency hyperbolic band. This contributes to a high

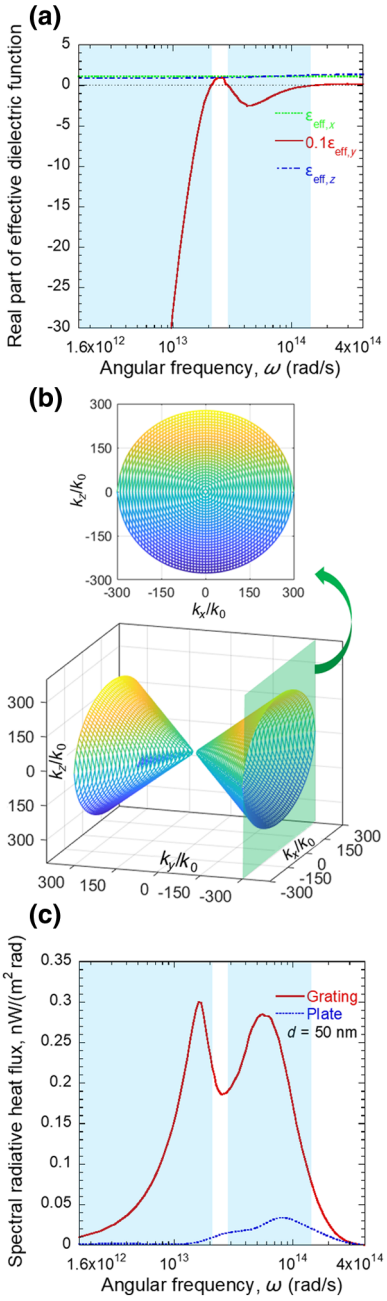

FIG. 4. (a) Effective dielectric functions (real parts only) of graphite gratings; (b) Isofrequency contour of effective biaxial media at $\omega = 1.3 \times 10^{14}$ rad/s; (c) Spectral radiative heat flux of graphite gratings and plates at $d = 50$ nm. The shaded regions indicate Type I hyperbolic bands of graphite gratings with default parameters of $f = 0.1$ and $P = 10$ nm.

SRHT in a broad band, leading to the higher NFRHF of graphite gratings.

In order to explain what contributes to the much larger SRHF and thus the higher NFRHF enabled by graphite gratings, Fig. 5 illustrates the energy transmission coefficient (ETC) distributions of graphite plates and gratings in the whole wavevector region. One peak frequency, i.e.,

$\omega = 1.6 \times 10^{13}$ rad/s, is chosen for analysis, while the other is not investigated here since the mechanism is similar. Other parameters are identical to those in Fig. 4(c). As can be seen in the figure, the high ETC of graphite gratings can reach a broad region with a tangential wavevector β larger than 600 k_0, while that of the counterpart plates is considerable only when β is lower than 30 k_0. In Fig. 5(a), the green solid line representing $k_x^2 + k_y^2 = k_0^2\sqrt{\varepsilon_e}$, beyond (below) which propagating (evanescent) waves are supported, is in great agreement with the high ETC region. Therefore, high-β evanescent waves from the vacuum become propagating in graphite plates. This demonstrates that conventional nonresonant Type II hyperbolic modes dominate the NFTR of graphite plates. For the graphite gratings shown in Fig. 5(b), anisotropic surface plasmon polaritons (SPPs) are excited here. This can be verified by the excellent agreement between the high ETC region and the green solid line, which represents the asymptote of the dispersion relation of anisotropic SPPs governed by Eq. (9). Different from conventional circles, the dispersion relation of anisotropic SPPs supported by graphite gratings graphs as a hyperbola, thus this anisotropic surface resonance is called hyperbolic SPPs (HSPPs). Type I anisotropic HSPPs render graphite gratings to harvest high ETC on broader wavevector regions and thus possess higher NFRHF than do counterpart plates.

C. Effects of orientation of graphite optical axis

For practical graphite, its optical axis may have different orientations relative to the surface plane. To consider this effect, Fig. 6(a) depicts the SRHF of graphite gratings ($f = 0.1$, $P = 10$ nm) and plates with different optical axis directions at $d = 50$ nm. Since plates along the x-y plane are infinite, their NFTR is the same for the optical axis along the x and y coordinates. As shown in the figure, the SRHF of graphite gratings with different optical axis directions, delineated by the red solid, green dash-dotted, and blue dashed lines, possesses similar shapes. Among them, the two peaks of the blue dashed line have the highest value, thus leading to the largest NFRHF of graphite gratings with an optical axis out of plane (i.e., along the z coordinate). Graphite plates support similar phenomenon, namely graphite plates with optical axes out of plane have a better performance in the NFTR than those with optical axes in plane, as shown by the pink dot and black double dash-dotted line. Note that the change of optical axes from the x coordinate to the z coordinate redshifts the high-frequency peak SRHF of graphite gratings. Contrary to the scheme of the in-plane optical axis, the peak SRHF at low frequency shows a higher magnitude than that at high frequency for the scheme of the out-of-plane optical axis.

To reveal the heat transfer mechanism in Figs. 6(a)–6(d), we plot the ETC distributions for graphite plates and gratings with different optical axis orientations at $\omega = 1.6 \times 10^{13}$ rad/s and the default geometry parameters. For graphite plates with in-plane optical axes, $\varepsilon_o = -628.9 + 687.5i$ and $\varepsilon_e = 0.4 + 19.6i$ at the selected frequency, so that the dispersion relation of surface resonant modes $(1 - \varepsilon_e\varepsilon_o)k_x^2 + (1 - \varepsilon_o^2)k_y^2 = -\varepsilon_e\varepsilon_o^2 k_0^2$ cannot be satisfied [52]. Only conventional nonresonant Type II hyperbolic modes are supported. This can be confirmed by the agreement of the high ETC region with the green solid line, which represents propagating waves in graphite plates, as shown in Fig. 6(b). The obscure distinction between propagating and evanescent waves is due to the high loss of graphite. When employing EMT, graphite gratings with x coordinate optical axes can be treated as uniaxial plates with the same

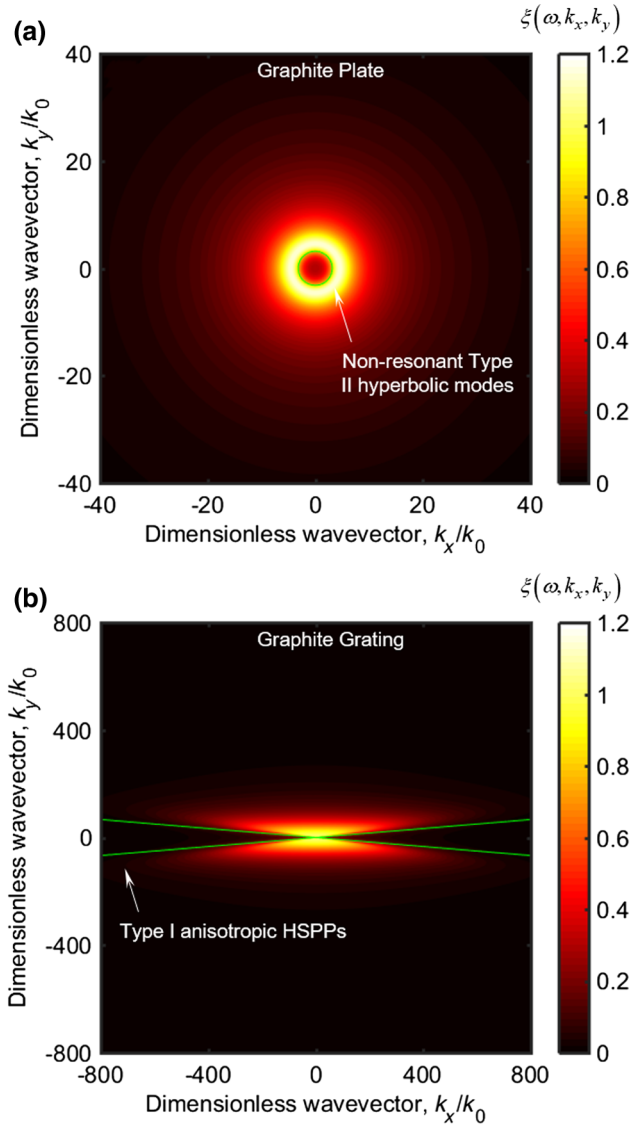

FIG. 5. Energy transmission coefficient distributions in the wavevector region at $\omega = 1.6 \times 10^{13}$ rad/s and $d = 50$ nm for (a) graphite plates and (b) graphite gratings ($f = 0.1$, $P = 10$ nm).

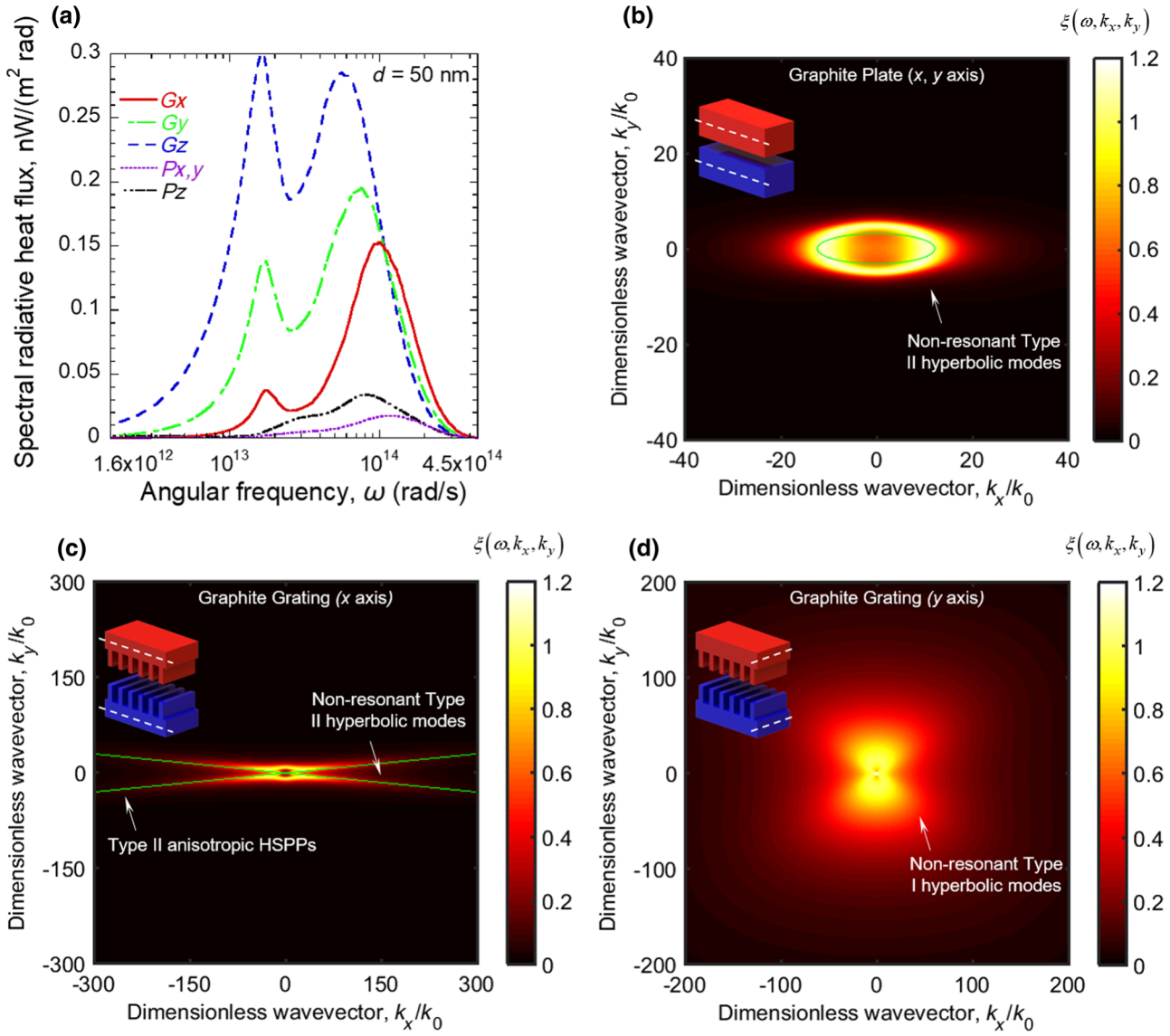

FIG. 6. (a) Spectral radiative heat flux of graphite plates and gratings with optical axes along x, y, and z coordinates; Energy transmission coefficient distributions at $\omega = 1.6 \times 10^{13}$ rad/s for (b) graphite plates with x coordinate optical axes, (c) graphite gratings with x coordinate optical axes, and (d) graphite gratings with y coordinate optical axes. Other parameters in the figures are $f = 0.1$, $P = 10$ nm, and $d = 50$ nm. White dashed lines in the inserts of Figs. 6(b)–6(d) denote optical axes of graphite.

optical axes, which are similar to the configuration in Fig. 6(b). However, Fig. 6(c) is very different. Type II anisotropic HSPPs are excited here, as identified by the coincidence of the high ETC region with the green solid lines representing asymptotes of the anisotropic SPPs' dispersion relation governed by Eq. (9). Interestingly, in the narrow region between green solid lines, where SPPs are not excited, high ETC is also supported. This is because k_y is very small there and has a high probability to be lower than $\sqrt{\varepsilon_e k_0^2 - k_x^2 \varepsilon_e/\varepsilon_o}$. Then, $k_{ze} = \sqrt{\varepsilon_e k_0^2 - k_x^2 \varepsilon_e/\varepsilon_o - k_y^2}$ can be real, which means that waves with high tangential wavevectors become propagating inside graphite gratings. Therefore, the frustrated total internal reflection, i.e., nonresonant hyperbolic modes, contributes to the high ETC in the narrow region. For graphite gratings with optical axes lying along the y coordinate, effective dielectric functions for this configuration are $\varepsilon_{\text{eff},x} > 0$, $\varepsilon_{\text{eff},y} > 0$, and $\varepsilon_{\text{eff},z} < 0$. These effective dielectric functions cannot allow Eq. (8), i.e., the dispersion relation of anisotropic SPPs, to be satisfied, and thus anisotropic surface resonant modes cannot be supported here. Nevertheless, nonresonant Type I hyperbolic modes still exist and generate a broad high-ETC region as shown in Fig. 6(d), giving rise to a considerable NFRHF.

IV. CONCLUSION

This paper investigates near-field thermal radiation between nanostructures comprised of natural anisotropic materials, namely gratings of graphite with different orientations of the optical axis. Based on exact scattering theories, graphite gratings with out-of-plane optical axes are found to support higher near-field radiative heat flux compared with those whose optical axes lie in plane. For the former scheme, with a filling factor of 0.1 and period of 10 nm, graphite gratings are demonstrated to possess sevenfold larger NFRHF than that of the counterpart plates at nanometric gap distances, outperforming blackbodies by more than four orders of magnitude. This prominent performance is mainly attributed to enhanced spectral radiative heat flux in a broad hyperbolic band. Corrugating changes the material dispersion of graphite plates from Type II to Type I. Anisotropic hyperbolic surface plasmon polaritons are also enabled in a broad frequency range, leading to the large NFRHT. With regard to graphite gratings with optical axes in plane, for optical axes parallel to the etching direction, NFRHT mainly comes from broadband Type II anisotropic HSPPs and nonresonant hyperbolic modes. For optical axes perpendicular to the etching direction, nonresonant Type I hyperbolic modes play a dominant role. This work sheds light on the near-field thermal radiation mechanism of nanostructures made of natural anisotropic materials, and may pave the way for efficient thermal management based on thermal radiation.

ACKNOWLEDGMENTS

The support from the National Natural Science Foundation of China (Grants No. 51706096, No. 51336003, and No. 51590901) is gratefully acknowledged. XL also wants to thank the support from Fundamental Research Funds for the Central Universities (Grant No. 56XIA17001).

[1] W. Cai, U. K. Chettiar, A. V. Kildishev, and V. M. Shalaev, Optical cloaking with metamaterials, Nat. Photonics **1**, 224 (2007).

[2] A. J. Hoffman, L. Alekseyev, S. S. Howard, K. J. Franz, D. Wasserman, V. A. Podolskiy, E. E. Narimanov, D. L. Sivco, and C. Gmachl, Negative refraction in semiconductor metamaterials, Nat. Mater. **6**, 946 (2007).

[3] E. Pop, D. Mann, Q. Wang, K. Goodson, and H. Dai, Thermal conductance of an individual single-wall carbon nanotube above room temperature, Nano Lett. **6**, 96 (2006).

[4] T. V. Teperik, F. J. García de Abajo, A. G. Borisov, M. Abdelsalam, P. N. Bartlett, Y. Sugawara, and J. J. Baumberg, Omnidirectional absorption in nanostructured metal surfaces, Nat. Photonics **2**, 299 (2008).

[5] G. C. R. Devarapu and S. Foteinopoulou, Broadband Near-Unidirectional Absorption Enabled by Phonon-Polariton Resonances in SiC Micropyramid Arrays, Phys. Rev. Applied **7**, 034001 (2017).

[6] J.-J. Greffet, R. Carminati, K. Joulain, J.-P. Mulet, S. Mainguy, and Y. Chen, Coherent emission of light by thermal sources, Nature **416**, 61 (2002).

[7] E. Rephaeli, A. Raman, and S. Fan, Ultrabroadband photonic structures to achieve high-performance daytime radiative cooling, Nano Lett. **13**, 1457 (2013).

[8] Z. M. Zhang, *Nano/Microscale Heat Transfer* (McGraw-Hill, New York, 2007).

[9] M. Francoeur, M. P. Mengüç, and R. Vaillon, Near-field radiative heat transfer enhancement via surface phonon polaritons coupling in thin films, Appl. Phys. Lett. **93**, 043109 (2008).

[10] S.-A. Biehs, E. Rousseau, and J.-J. Greffet, Mesoscopic Description of Radiative Heat Transfer at the Nanoscale, Phys. Rev. Lett. **105**, 234301 (2010).

[11] Y. Xuan, An overview of micro/nanoscaled thermal radiation and its applications, Photonics Nanostruct. Fundam. Appl. **12**, 93 (2014).

[12] X. L. Liu, L. P. Wang, and Z. M. Zhang, Near-field thermal radiation: Recent progress and outlook, Nanosc. Microsc. Therm. **19**, 98 (2015).

[13] M. Lim, S. S. Lee, and B. J. Lee, Near-field thermal radiation between doped silicon plates at nanoscale gaps, Phys. Rev. B **91**, 195136 (2015).

[14] M. P. Bernardi, D. Milovich, and M. Francoeur, Radiative heat transfer exceeding the blackbody limit between macroscale planar surfaces separated by a nanosize vacuum gap, Nat. Commun. **7**, 12900 (2016).

[15] J. I. Watjen, B. Zhao, and Z. M. Zhang, Near-field radiative heat transfer between doped-Si parallel plates separated by a spacing down to 200 nm, Appl. Phys. Lett. **109**, 203112 (2016).

[16] Y. Ge, Y. Jiang, and M. Yungui, Near-field heat transfer between graphene monolayers: Dispersion relation and parametric analysis, Appl. Phys. Express **9**, 122001 (2016).

[17] S. Edalatpour, J. DeSutter, and M. Francoeur, Near-field thermal electromagnetic transport: An overview, J. Quant. Spectrosc. Radiat. Transfer **178**, 14 (2016).

[18] L. Cui, W. Jeong, V. Fernández-Hurtado, J. Feist, F. J. García-Vidal, J. C. Cuevas, E. Meyhofer, and P. Reddy, Study of radiative heat transfer in Ångström- and nanometre-sized gaps, Nat. Commun. **8**, 14278 (2017).

[19] J. Dong, J. Zhao, and L. Liu, Radiative heat transfer in many-body systems: Coupled electric and magnetic dipole approach, Phys. Rev. B **95**, 125411 (2017).

[20] J. Song and Q. Cheng, Near-field radiative heat transfer between graphene and anisotropic magneto-dielectric hyperbolic metamaterials, Phys. Rev. B **94**, 125419 (2016).

[21] B. Guha, C. Otey, C. B. Poitras, S. Fan, and M. Lipson, Near-field radiative cooling of nanostructures, Nano Lett. **12**, 4546 (2012).

[22] J. Peng, G. Zhang, and B. Li, Thermal management in MoS2 based integrated device using near-field radiation, Appl. Phys. Lett. **107**, 133108 (2015).

[23] V. B. Svetovoy and G. Palasantzas, Graphene-on-Silicon Near-Field Thermophotovoltaic Cell, Phys. Rev. Applied **2**, 034006 (2014).

[24] M. Ghashami, S. K. Cho, and K. Park, Near-field enhanced thermionic energy conversion for renewable energy recycling, J. Quant. Spectrosc. Radiat. Transfer **198**, 59 (2017).
[25] P. Ben-Abdallah and S.-A. Biehs, Contactless heat flux control with photonic devices, AIP Adv. **5**, 053502 (2015).
[26] A. Wang, Z. Zheng, and Y. Xuan, Near-field radiative thermal control with graphene covered on different materials, J. Quant. Spectrosc. Radiat. Transfer **180**, 117 (2016).
[27] X. Liu, J. Shen, and Y. Xuan, Pattern-free thermal modulator via thermal radiation between Van der Waals materials, J. Quant. Spectrosc. Radiat. Transfer **200**, 100 (2017).
[28] Z. Zheng, X. Liu, A. Wang, and Y. Xuan, Graphene-assisted near-field radiative thermal rectifier based on phase transition of vanadium dioxide (VO_2), Int. J. Heat Mass Transfer **109**, 63 (2017).
[29] M. Elzouka and S. Ndao, Meshed doped silicon photonic crystals for manipulating near-field thermal radiation, J. Quant. Spectrosc. Radiat. Transfer **204**, 56 (2018).
[30] T. G. Habteyes, I. Staude, K. E. Chong, J. Dominguez, M. Decker, A. Miroshnichenko, Y. Kivshar, and I. Brener, Near-field mapping of optical modes on all-dielectric silicon nanodisks, ACS Photonics **1**, 794 (2014).
[31] Y. Sugawara, J. Yamanishi, T. Tokuyama, Y. Naitoh, and Y. J. Li, Atomic-Resolution Imaging of the Optical Near Field Based on the Surface Photovoltage of a Silicon Probe Tip, Phys. Rev. Applied **3**, 044020 (2015).
[32] S. F. Becker, M. Esmann, K. Yoo, P. Gross, R. Vogelgesang, N. Park, and C. Lienau, Gap-plasmon-enhanced nanofocusing near-field microscopy, ACS Photonics **3**, 223 (2016).
[33] E. Sakat, V. Giliberti, M. Bollani, A. Notargiacomo, M. Pea, M. Finazzi, G. Pellegrini, J. Hugonin, A. Weber-Bargioni, M. Melli, et al., Near-Field Imaging of Free Carriers in ZnO Nanowires with a Scanning Probe Tip Made of Heavily Doped Germanium, Phys. Rev. Applied **8**, 054042 (2017).
[34] K. Ito, K. Nishikawa, H. Iizuka, and H. Toshiyoshi, Experimental investigation of radiative thermal rectifier using vanadium dioxide, Appl. Phys. Lett. **105**, 253503 (2014).
[35] R. Guérout, J. Lussange, F. S. S. Rosa, J. P. Hugonin, D. A. R. Dalvit, J. J. Greffet, A. Lambrecht, and S. Reynaud, Enhanced radiative heat transfer between nanostructured gold plates, Phys. Rev. B **85**, 180301 (2012).
[36] X. Liu, R. Zhang, and Z. Zhang, Near-field radiative heat transfer with doped-silicon nanostructured metamaterials, Int. J. Heat Mass Transfer **73**, 389 (2014).
[37] B. Liu, J. Shi, K. Liew, and S. Shen, Near-field radiative heat transfer for Si based metamaterials, Opt. Commun. **314**, 57 (2014).
[38] J.-Y. Chang, Y. Yang, and L. Wang, Enhanced energy transfer by near-field coupling of a nanostructured metamaterial with a graphene-covered plate, J. Quant. Spectrosc. Radiat. Transfer **184**, 58 (2016).
[39] K. Shi, F. Bao, and S. He, Enhanced near-field thermal radiation based on multilayer graphene-hBN heterostructures, ACS Photonics **4**, 971 (2017).
[40] W. Chihhui, N. Burton, III, J. Jeremy, M. Andrew, Z. Byron, S. Steve, and S. Gennady, Metamaterial-based integrated plasmonic absorber/emitter for solar thermo-photovoltaic systems, J. Optics **14**, 024005 (2012).
[41] Y. X. Yeng, W. R. Chan, V. Rinnerbauer, J. D. Joannopoulos, M. Soljačić, and I. Celanovic, Performance analysis of experimentally viable photonic crystal enhanced thermophotovoltaic systems, Opt. Expr. **21**, A1035 (2013).
[42] B. Zhao, L. Wang, Y. Shuai, and Z. M. Zhang, Thermophotovoltaic emitters based on a two-dimensional grating/thin-film nanostructure, Int. J. Heat Mass Transfer **67**, 637 (2013).
[43] J.-Y. Chang, Y. Yang, and L. Wang, Tungsten nanowire based hyperbolic metamaterial emitters for near-field thermophotovoltaic applications, Int. J. Heat Mass Transfer **87**, 237 (2015).
[44] A. Ghanekar, J. Ji, and Y. Zheng, High-rectification near-field thermal diode using phase change periodic nanostructure, Appl. Phys. Lett. **109**, 123106 (2016).
[45] J. Shen, X. Liu, H. He, W. Wu, and B. Liu, High-performance noncontact thermal diode via asymmetric nanostructures, J. Quant. Spectrosc. Radiat. Transfer **211**, 1 (2018).
[46] J. Watjen, X. Liu, B. Zhao, and Z. Zhang, A computational simulation of using tungsten gratings in near-field thermophotovoltaic devices, J. Heat Transfer **139**, 052704 (2017).
[47] S. A. Biehs, F. S. S. Rosa, and P. Ben-Abdallah, Modulation of near-field heat transfer between two gratings, Appl. Phys. Lett. **98**, 243102 (2011).
[48] R. Guérout, J. Lussange, H. B. Chan, A. Lambrecht, and S. Reynaud, Thermal Casimir force between nanostructured surfaces, Phys. Rev. A **87**, 052514 (2013).
[49] H. R. Philipp, Infrared optical properties of graphite, Phys. Rev. B **16**, 2896 (1977).
[50] B. Draine and H. M. Lee, Optical properties of interstellar graphite and silicate grains, Astrophys. J. **285**, 89 (1984).
[51] F. S. S. Rosa, D. A. R. Dalvit, and P. W. Milonni, Casimir interactions for anisotropic magnetodielectric metamaterials, Phys. Rev. A **78**, 032117 (2008).
[52] X. Liu and Y. Xuan, Super-Planckian thermal radiation enabled by hyperbolic surface phonon polaritons, Sci. China Technol. Sci. **59**, 1680 (2016).
[53] X. Wang, S. Basu, and Z. Zhang, Parametric optimization of dielectric functions for maximizing nanoscale radiative transfer, J. Phys. D: Appl. Phys. **42**, 245403 (2009).
[54] X. Liu, B. Zhao, and Z. M. Zhang, Enhanced near-field thermal radiation and reduced Casimir stiction between doped-Si gratings, Phys. Rev. A **91**, 062510 (2015).
[55] J. J. Loomis and H. J. Maris, Theory of heat transfer by evanescent electromagnetic waves, Phys. Rev. B **50**, 18517 (1994).
[56] S.-A. Biehs, M. Tschikin, and P. Ben-Abdallah, Hyperbolic Metamaterials as an Analog of a Blackbody in the Near Field, Phys. Rev. Lett. **109**, 104301 (2012).
[57] X. Liu and Z. Zhang, Near-field thermal radiation between metasurfaces, ACS Photonics **2**, 1320 (2015).
[58] X. Liu, R. Zhang, and Z. Zhang, Near-field thermal radiation between hyperbolic metamaterials: Graphite and carbon nanotubes, Appl. Phys. Lett. **103**, 213102 (2013).
[59] D. R. Smith and D. Schurig, Electromagnetic Wave Propagation in Media with Indefinite Permittivity and Permeability Tensors, Phys. Rev. Lett. **90**, 077405 (2003).